Single-Pixel Ensemble Correlation Algorithm for Boundary Measurement on Axisymmetric Boattail Surface

Tran The Hung

December 28, 2021

SINGLE-PIXEL ENSEMBLE CORRELATION ALGORITHM FOR BOUNDARY MEASUREMENT ON AXISYMMETRIC BOATTAIL SURFACE

Tran The Hung[*]

Le Quy Don Technical University

Abstract

Particle image velocimetry (PIV) measurement is an important technique in analyzing velocity fields. However, in traditional cross-correlation algorithm, the resolution of velocity fields is limited by the size of interrogation windows and the boundary layer was not captured well. In this study, single-pixel ensemble correlation algorithm was applied to analyze flow near the surface of an axisymmetric boattail model. The initial images data was obtained by experimental methods with the setup of PIV measurement. The results showed that the new algorithm was considerably improved resolution of flow fields near the surface and could be used to measure boundary-layer profile. Detailed characteristics of boundary-layer profile at different flow conditions were discussed. Interestingly, boundary-layer profile does not change much before the shoulder. However, the size of separation bubble on the boattail surface highly decreases with increasing Reynolds number. The study provides initial results of flow fields, which could be useful for further investigation of drag reduction by numerical and experimental techniques.

Keywords: Single-pixel ensemble correlation; PIV measurement; boattail model; boundary layer.

1. Introduction

Reducing base drag and improving performance of the blunt-base vehicle is a big challenge for aerodynamic and fluid researchers in many years. Among of many devices for drag reductions such as base bleed, lock-vortex afterbody, splitter plate, base cavity and boattail model, the boattail model shows high effective [1]. A boattail model is determined as an additional contour shape added to blunt base model. In fact, the boattail model was widely applied for missiles and projectiles at high speed flow [2, 3]. However, flow behavior around the boattail model and its effect on drag reduction of model is not fully understood at low-speed conditions [3, 4].

Major studies of flow behavior around the boattail model at low speed were conducted by Mair [1, 3]; Buresti [5]; Mariotti et al. [6, 7] and Tran et al. [8, 9, 10]. The results indicated that the flow around boattail models at low speed shows many different

---

[*] Email: thehungmfti@gmail.com

features to that of high speed. Additionally, since flow around the base is very sensitive to disturbance at low speed condition, measurement the boundary-layer profile of boattail model is significantly complicated. Generally, it is a big challenge for both experimental technique and data processing. Consequently, improving measurement and data processing techniques are essential for further discussion of flow behavior and drag reduction strategy.

Particle image velocimetry (PIV) measurement provides a potential technique in analyzing velocity fields [11]. In fact, PIV measurement is a non-instrusive measurement technique, which does not disturb the flow fields. The working principle of PIV measurement technique is to measure the displacement of small tracer particles over a short time interval. For data processing, cross-correlation algorithm is applied for small interrogation window in the first and second frames. The size of interrogation window often ranges from 8×8 pixels to 64×64 pixels, which reduces the resolution of the velocity fields. Additionally, since the interrogation windows could cover the wall region, the boundary-layer profile is not captured correctly. One way to improve the results is to zoom-in boundary region and to repeat experiments for different areas. Clearly, that process requires high effort and consumes a lot of time.

The purpose of the current study is to apply a novel data processing technique for analyzing boundary layer of axisymmetric boattail model. In details, single-pixel ensemble correlation algorithm, which was proposed by Westerweel et al. [12], is applied to obtain high resolution of the flow fields near the wall. In fact, the algorithm was applied in previous studies for micro-PIV measurement and was validated by Kahler et al. [13]. However, the application for boundary-layer measurement of axisymmetric boattail was not illustrated. We will use the data of tranditional cross-correlation algorithm far from the wall to validate results of the current methods. This study shows that both algorithms provide good results for flow far from the wall. Additionally, the velocity profiles near the wall by single-pixel ensemble correlation are much improved by comparison to that of traditional cross-correlation algorithms. Consequently, PIV measurement with single-pixel ensemble correlation algorithm provides a promising tool to measure the boundary layer of moving object. The flow behavior around boattail model of 20º and its boundary-layer thickness at different Reynolds number will be discussed in detail in this study. Processing results could be used as initial data for further investigation of afterbody flow by both numerical and experimental methods.

2. Experimental setup

The experimental setup was similar to the one by Tran et al. [8, 10]. In the measurement, axisymmetric boattail model was supported in wind tunnel by a strut with cross section of NACA 0018. The diameter D of the model is 30 mm and the total length L is 251 mm. At the end the cylinder part, a conical boattail with fixed length of $L_b = 0.7 D$ and angle of $\beta = 20º$ was added (Fig. 1).
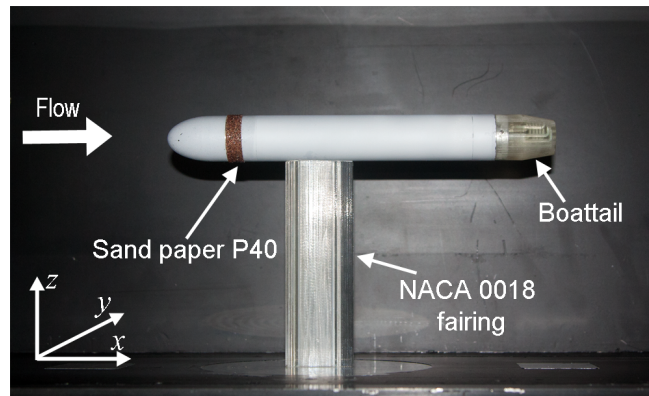

Fig. 1. Model in wind tunnel test

For PIV measurement, a laser was placed on the top to illuminate particles in the test section. Double-pulsed Nd-YLF Laser (LDY-303, 527 nm, Litron Lasers) was employed for the experiments. Laser sheet is setup at minimum thickness, which was around 1 mm. Time interval between double frame was varied by speed of wind tunnel in the range from 4 µs to 8 µs. The maximum movement of particles in images of a double frame was around 6 pixels.

For generating luminescent particles inside test section, smoke generator LSG-500S was employed. The smoke generator has five laskin nozzles and can provide air with smoke particles of around 1 µm in diameter and 25 m³/h in volume.

A high-speed camera Phantom V611 was placed on one side of test section to record particles movements around the model. The camera had a resolution of 1280×800 pixels and was equipped with a Nikon lens 100 mm f2.8. Additionally, an extension tube (36 mm) was also placed in front of the lens to increase magnification of the measurement section. The camera angle with dimensions of 40 mm × 25 mm was illustrated by red dashed line as shown in Fig. 2. The resolution of image reached around 32.5 pixels/mm. In addition, the camera was setup at 600 fps and movement of particles was recorded at around 9 s.

Experiments were conducted at four different velocities from 22 m/s to 45 m/s, which gave the based-diameter Reynolds number from 4.34×10^4 to 8.89×10^4.
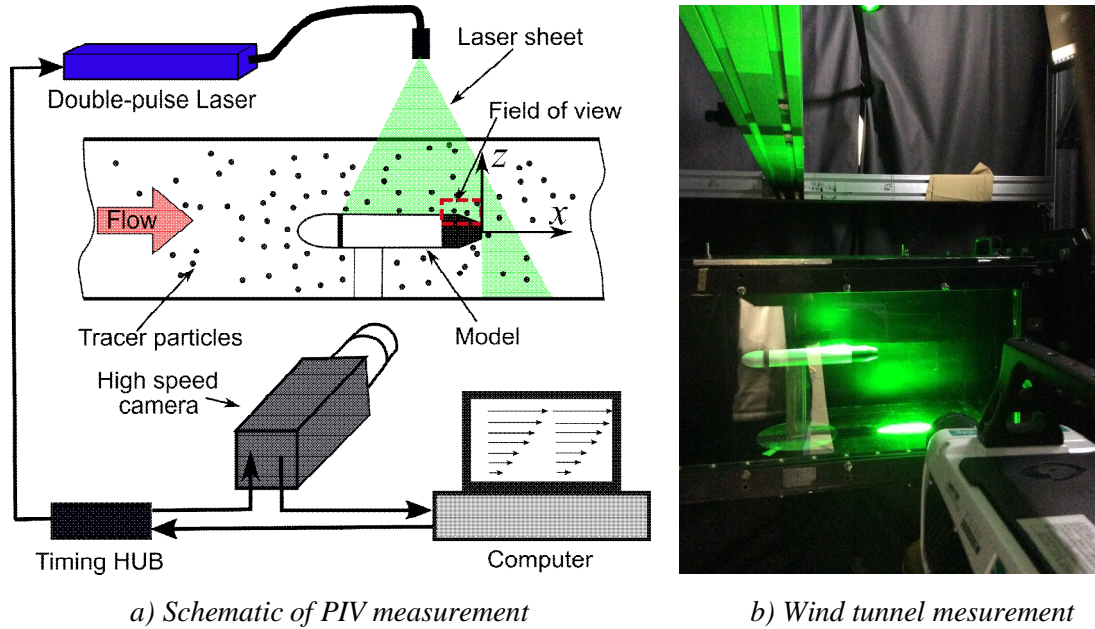

| *a) Schematic of PIV measurement* | *b) Wind tunnel mesurement* |

Fig. 2. Setup of PIV measurement and wind tunnel test for flow velocity measurement

3. Measurement technique

For data processing, the cross-correlation algorithm divides the first image into small interrogation areas (interrogation windows). After that, the cross-correlations of those windows with the second image are calculated. The position of maximum cross-correlation shows the displacement of the interrogation windows in the second images. Since the time interval between the first and second images were known and displacement of interrogation windows was calculated, the velocity fields can be obtained. The formula for cross-correlation is shown as:

$$R(s) = \int_W I_1(X) I_2(X + s) dX \tag{1}$$

where I_1 and I_2 present the first and second image, X is the coordinate, W is the size of interrogation window and s is the displacement. As the velocity of each interrogation windows is obtained, velocity fields of the whole image could be constructed. The method allows obtaining instantaneous velocity field from two images at different small time. By averaging instantaneous values at different time interval, the mean velocity fields can be found.

The size of the interrogation window often ranges from 8×8 pixels to 64×64 pixels. Obviously, it reduces the resolution of velocity fields by comparison to image data. Additionally, it is very difficult to capture the flow fields near the wall, where the number of particles is significantly limited and the interrogation windows contain boundary of models and free air.

To overcome the disadvantage of the cross-correlation algorithm, the single-pixel resolution ensemble correlation algorithm is used for data processing. The algorithm calculates cross-correlation coefficient for a single position of the first image and the interrogation windows in the second image from a group of double frames [12]. In more detail, information of each pixel in the first serial images and second serial images from a huge number of images was collected. Then, cross-correlation of each pixel in the first images with the second images was calculated. As the results, the displacement of each pixel in the first serial images can be found and velocity fields can be obtained. Clearly, by comparison to cross-correlation algorithm which uses spatial domain, the single-pixel resolution ensemble correlation uses temporal domain for calculating displacement of the particles. To obtain the highly accurate results, a large number of double frames is requested. Since single pixel is processed separately, the resolution of velocity fields is the same with the size of image. Additionally, flow near the wall is measured highly accurate. The principles of the cross-correlation algorithm and the single-pixel ensemble correlation are shown in Fig. 3.
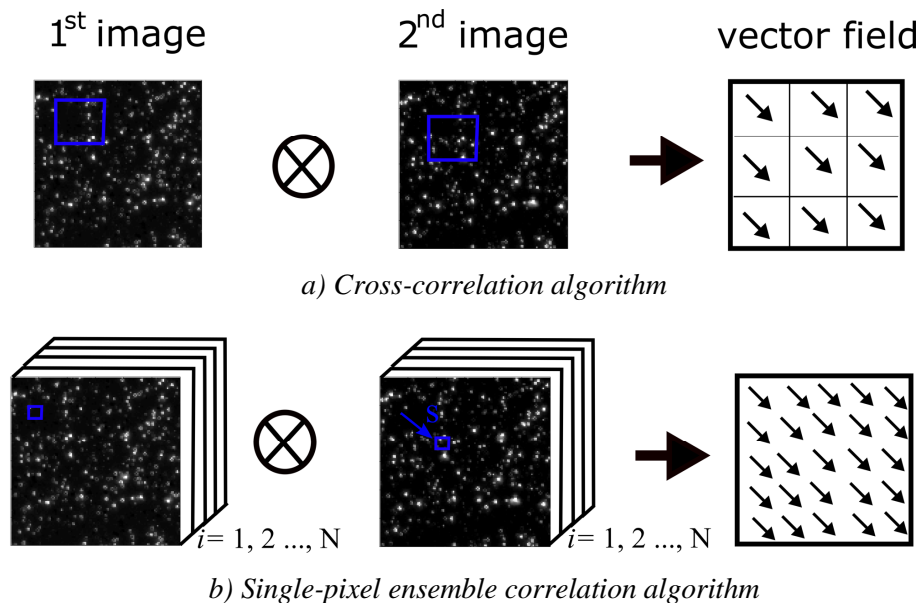

a) Cross-correlation algorithm

b) Single-pixel ensemble correlation algorithm

Fig. 3. Conventional and single-pixel ensemble correlation algorithm for data processing

The formula of cross-correlation in single-pixel ensemble correlation algorithm is shown as:

$$R(s) = \frac{1}{N} \sum_{i=1}^{N} I_1^{(i)}(X) I_2^{(i)}(X + s) \tag{2}$$

where N is the total number of double image. In this study, 5400 double-frame images are processed to obtain the average velocity field. Since the maximum displacement of particles from first to second frames is around 6 pixels, the displacement of each pixel in the first images was searched in a surrounding window of 25×25 pixels in the second image frames to reduce calculated time.

4. Results and discussions

4.1. Comparison between cross-correlation and single-pixel algorithms

Figure 4 presents streamwise velocity fields around the boattail model at Reynolds number of $Re = 4.34 \times 10^4$. Here, the x-axis was normalized by boattail length while the z-axis was normalized by diameter of model. Both methods provide sufficiently good results far from the model. However, cross-correlation algorithm shows unclear results near the shoulder and around the edges of image. Clearly, cross-correlation algorithm shows some uncertain results near the borderlines, as it was discussed in Section 3. The results were improved largely by single-pixel ensemble correlation method, where clear velocity fields were illustrated. Consequently, the single-pixel ensemble correlation algorithm shows highly effective in determining flow behavior near the surface of model.
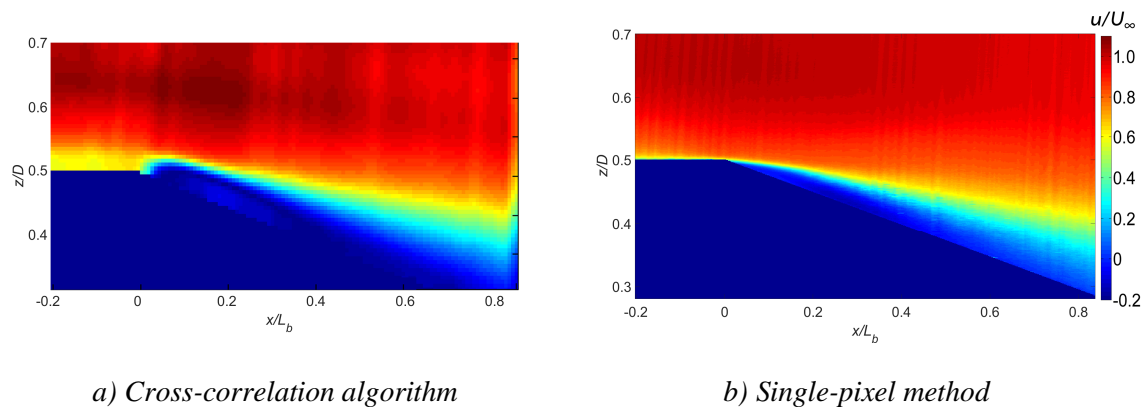

a) Cross-correlation algorithm   *b) Single-pixel method*

Fig. 4. Velocity fields in two measurement methods at Re = 4.34×10⁴

A comparison of the boundary-layer profile at x/D = -0.2 (6 mm before the shoulder) are shown in Fig. 5. The y-axis shows distance from the wall of the model. At 7 mm above the boattail surface, the velocity profile of two measurement methods is highly consistent. However, cross-correlation algorithm did not capture well the

boundary layer near the wall. It can be explained that the interrogation window covers the wall region and processing results are affected. In the opposite site, the single-pixel ensemble correlation algorithm improved remarkably the velocity profile.
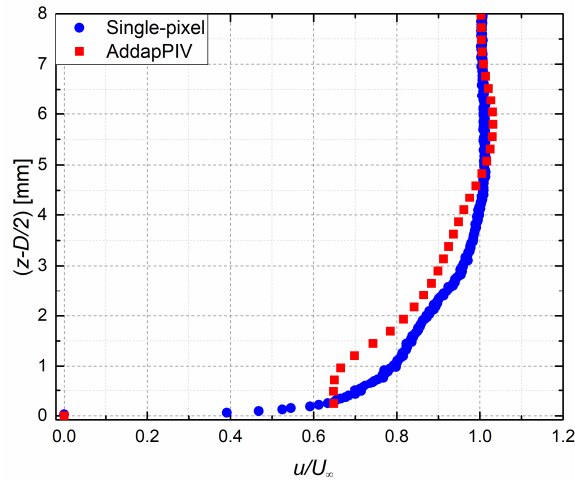

Fig. 5. Boundary-layer profile from two algorithms
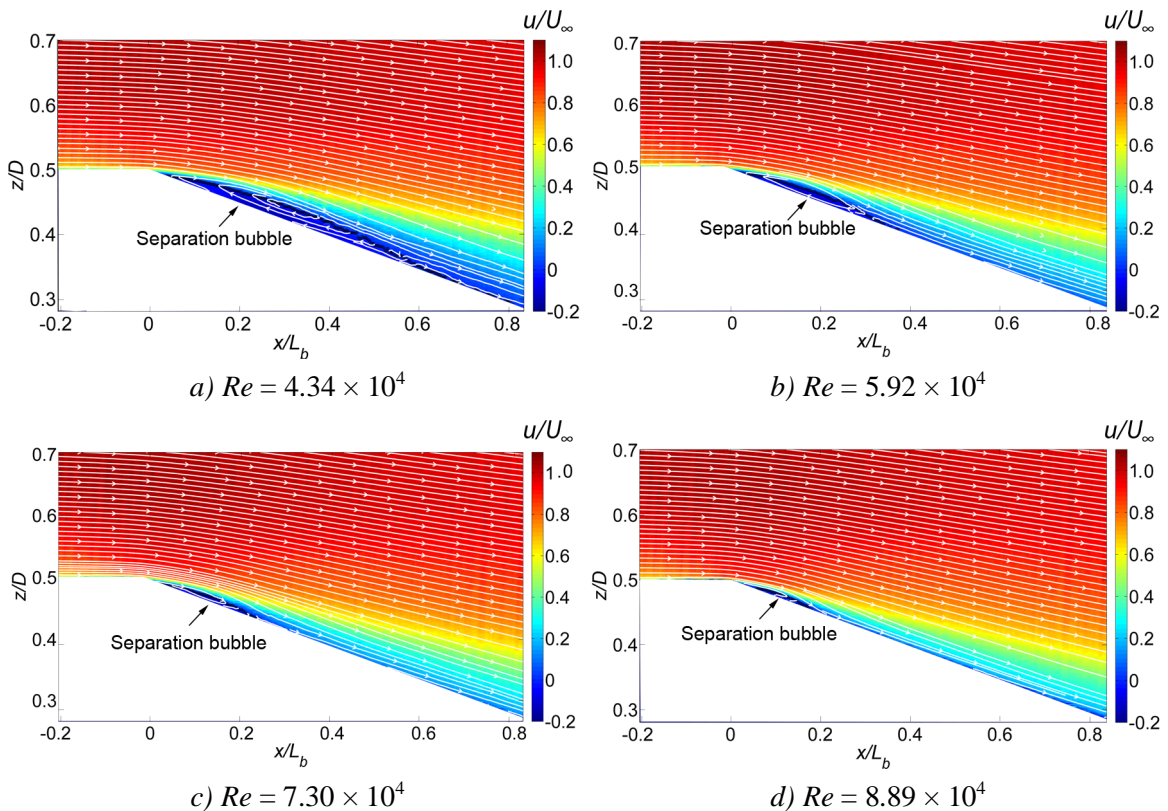
4.2. Mean velocity fields

a) $Re = 4.34 \times 10^4$

b) $Re = 5.92 \times 10^4$

c) $Re = 7.30 \times 10^4$

d) $Re = 8.89 \times 10^4$

Fig. 6. Streamwise velocity fields on symmetric vertical plan at $\beta = 20°$

85

The mean flow velocity in the vertical plane was shown in Fig. 6 for different flow conditions. The black dots show position of zero velocity streamline (dividing streamline). For all case, the flow is highly bent around the shoulder, which is affected by boattail geometry. A small separation bubble region is observed on the surface. Interestingly, the size of separation bubble decreases quickly with increasing Reynolds number from $Re = 4.34 \times 10^4$ to $Re = 8.89 \times 10^4$. At Reynolds number around $Re = 8.89 \times 10^4$, separation bubble region becomes narrow and flow above the boattail is mainly affected by the geometry. It is expected that the separation bubble will be disappeared at higher Reynolds number or high Mach number conditions. The separation bubble flow is, therefore, a typical regime at low-speed conditions and was captured well by the single-pixel ensemble correlation algorithm. Note that previous study by Lavrukhin and Popovich [14] did not show a separation bubble for a wide range of Mach number conditions.

4.3. Characteristics of separation and reattachment on the boattail surface
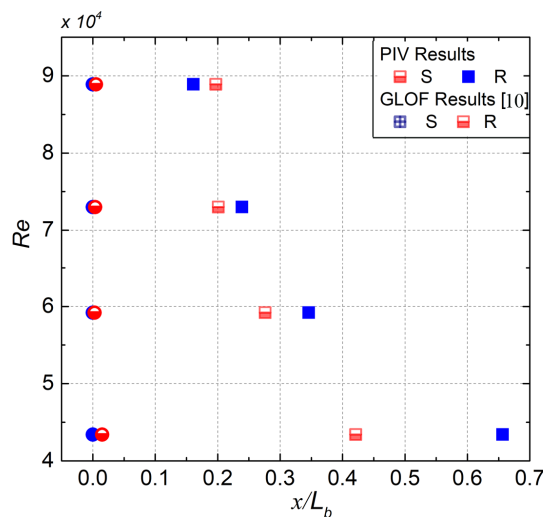

Fig. 7. Separation and reattachment positions on boattail surface at different Reynolds number conditions (S is separation position, R is reattachment position)

Figure 7 shows separation and reattachment position on the boattail surface by PIV measurement and global luminescent oil film (GLOF) skin-friction measurement, which was obtained from previous study by Tran et al. [10]. The GLOF measurement captured skin-friction fields on the surface by a luminescent oil-film layer. The separation and reattachment positions by PIV measurement are determined by streamwise velocity along the boattail surface changing to negative and positive, respectively. The separation positions in both two methods show analogous results. At high Reynolds numbers, reattachment positions present similar results for two methods. However, at Reynolds number around $Re = 4.34 \times 10^4$, results of both methods show

remarkably different. It can be explained that the movement of air near reattachment position at low speed ($Re = 4.34 \times 10^4$) is sufficient small and the number of particles near the boattail surface is not enough to obtain good data for PIV measurement processing. Additionally, due to unsteady behavior, the reattachment is often formed a large region on the surface.

4.4. Boundary-layer velocity profiles

Figure 8 shows the boundary-layer profile for different Reynolds numbers tested at x/L_b = -0.2 (6 mm before the shoulder). The velocity profiles are averaged from 10 pixels surrounding measurement point in horizontal direction. Boundary-layer thickness δ is identified by a distance from wall surface to the position where streamwise velocity reaches to 95% free-stream velocity. The boundary-layer thickness is around δ = 2.8 mm and changes slightly for different flow conditions.
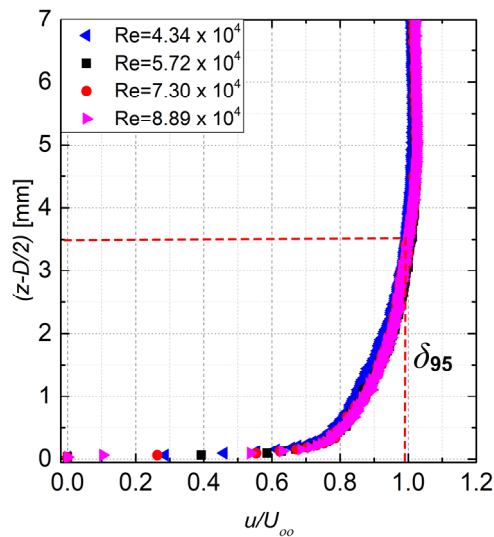

Fig. 8. Boundary measurement at different Reynolds number

As boundary-layer profiles are obtained, the displacement thickness δ^*, momentum thickness θ and shape factor H can be calculated. Those parameters are shown by below equations:

$$\delta^* = \int_0^\infty \left(1 - \frac{u(z)}{U_\infty}\right)dz, \qquad \theta = \int_0^\infty \frac{u(z)}{U_\infty}\left(1 - \frac{u(z)}{U_\infty}\right)dz, \qquad H = \frac{\delta^*}{\theta} \qquad (3)$$

The laminar boundary layer is characterized by the shape factor around H = 2.59 (Blasius boundary layer), while the turbulent boundary layer is characterized by H = 1.3-1.4.

Table 1 shows boundary-layer parameters at Reynolds number of $Re = 4.34 \times 10^4$. Clearly, boundary layer is fully turbulent before shoulder, which is shown by a shape factor of around $H = 1.3$.

Table 1. Characteristics of boundary layer

δ_{99}/D	δ^*/D	θ/D	H
0.0933	0.0180	0.0134	1.34

Figure 9 shows boundary-layer profiles at different positions on the boattail surfaces for two cases of Reynolds numbers $Re = 4.34 \times 10^4$ and $Re = 8.89 \times 10^4$. The black dashed line presents dividing streamline at $Re = 4.34 \times 10^4$. Clearly, the thickness of separation bubble at low Reynolds number is very high, which can be observed clearly from boundary-layer profile. However, separation bubble becomes smaller at high Reynolds number and it is not clearly illustrated. The figure also indicates that the thickness of boundary layer increases largely on the rear part of boattail model. Clearly, increasing thickness of boundary layer leads to a decreasing suction behind the base. Consequently, base drag of boattail model decreases.
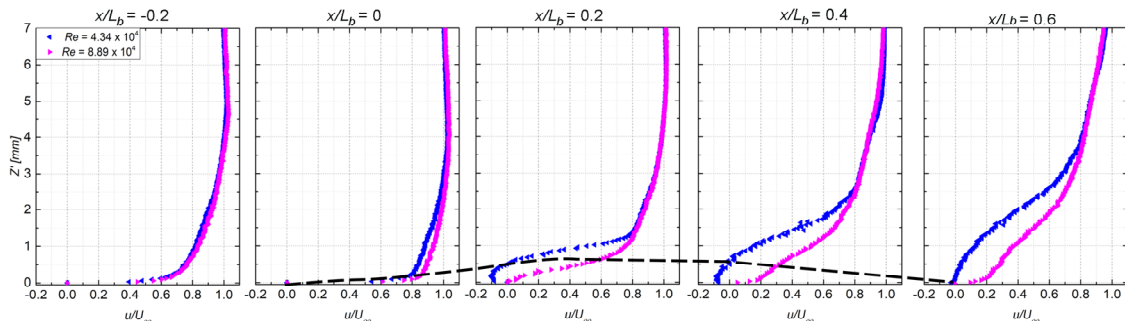

Fig. 9. Boundary profile at different positions on the boattail surface

The relative thickness of boundary layer at different positions was shown in the Fig. 10 for two Reynolds number of $Re = 4.34 \times 10^4$ and $Re = 8.89 \times 10^4$. The different boundary-layer thickness at $x/L_b = -0.2$ is small, as it was indicated before. However, boundary-layer thickness changes quickly near the shoulder and in the boattail surface. As the Reynolds number increases, the separation bubble becomes smaller and the thickness of boundary layer near the shoulder is reduced. In fact, the changes of boundary-layer thickness occurred before the shoulder, which is caused by increasing streamwise velocity. However, at $x/L_b > 0.2$, the thickness of boundary layer increases

with Reynolds number. Clearly, at high Reynolds number, the kinetic energy is remarkably lost on the boattail region and velocity recovery is lower. The high thickness of boundary layer near the base edge leads to a weaker near-wake and a decrease of base drag [15]. The results of boundary-layer profile also show some unsmooth changes near the base edge. It occurs from unperfected smooth of glass window, which uses to cover the test section of wind tunnel. To improve the results, further experiment should be conducted. However, this region is far from shoulder and does not affect our discussions.
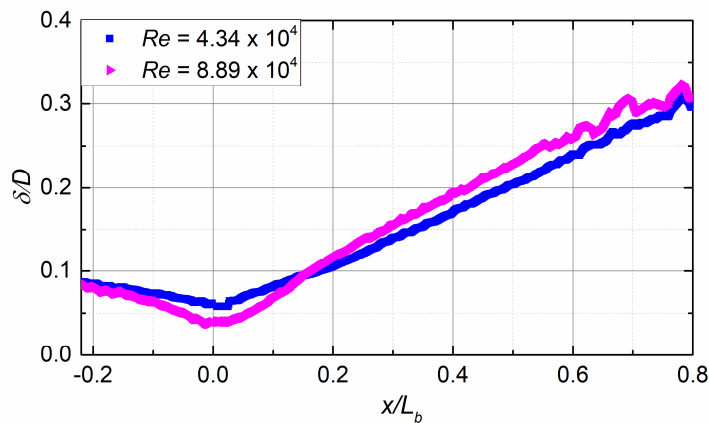

Fig. 10. Boundary-layer thickness

4.5. Skin-friction examination

For turbulent flow in a smooth wall and non-pressure gradient, a log-law region exists above the buffer layer. In this region, the velocity changes as a logarithmic function of distance to wall surface [16]. The existence of the logarithmic law allows estimation of wall shear stress of the model. In more details, relation among those parameters is shown as:

$$u^+ = \frac{1}{\kappa} \ln z^+ + C^+ \tag{4}$$

where $u^+ = \dfrac{u}{u_\tau}$, $z^+ = \dfrac{z u_\tau}{\nu}$ are non-dimensional velocity and distance from the wall and

$u_\tau = \sqrt{\dfrac{\tau_w}{\rho}}$ is the friction velocity.

The empirical constants $\kappa = 0.41$ and $C^+ = 5.0$ are selected for this study. Since boundary layer velocity was acquired from PIV measurement, Eq. (4) allows estimating

wall shear stress of the model with some offsets. Then, skin-friction coefficient C_{fx} is calculated by the below equation (5):

$$C_{fx} = 2\tau_w / (\rho U_\infty^2) \tag{5}$$

The results of logarithmic fitted lines are shown in Fig. 11 for different Reynolds number. Clearly, experimental data is fitted well in log-law region. The skin-friction coefficients are listed in Tab. 2. Skin friction reduces slightly when Reynolds number increases.

Table 2 also listed a simple estimation skin-friction coefficient using theoretical formula $c_{fx,fp} = 0.0263 / \mathrm{Re}_x^{1/7}$ for a flat plate. As can be seen, a high consistency between two measurements is obtained. The maximum difference between the skin-friction coefficient estimated by the log-law method with the one by theoretical methodology is around 1% at $Re = 7.30 \times 10^4$. One reason for this is from the high pressure gradient near the shoulder.
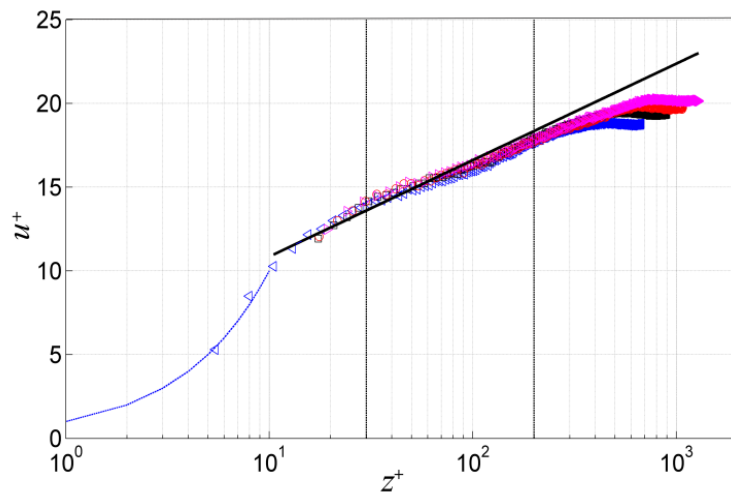

Fig. 11. Profiles of mean velocity for various Reynolds number

Tab. 2. Skin-friction coefficient at different Reynolds number

Reynolds number ($\times 10^4$)	4.34	5.92	7.30	8.89
C_{fx} ($\times 10^{-3}$)	5.61	5.32	5.09	4.88
$C_{fx,fp}$ ($\times 10^{-3}$)	5.65	5.33	5.13	4.90

5. Conclusions

In this study, velocity fields on axisymmetric boattail model at different Reynolds numbers were measured experimentally using single-pixel ensemble correlation algorithm. Major conclusions of the study are as bellow:

- The single-pixel ensemble correlation algorithm improves remarkably results of velocity fields and resolution of boundary-layer profile near the model surface by comparison to cross-correlation algorithm. Additionally, the single-pixel ensemble correlation algorithm is able to obtain accurate results of separation and reattachment positions at high Reynolds number. The results from the method are sufficient for estimating skin friction in non-pressure gradient region.

- Flow fields on the boattail surface are characterized by a separation bubble. The flow with separation bubble is a typical regime at low-speed condition and it was captured well by single-pixel ensemble correlation algorithm. The size of separation bubble highly decreases with increasing Reynolds number.

- Boundary-layer profiles do not change much in the region of $x/L_b < $ -0.2. However, increasing Reynolds number leads to a large decrease of boundary-layer thickness near the shoulder and increase of boundary-layer thickness in the reattachment region. Results of boundary-layer profile could be useful for further investigation of afterbody flow and drag control strategy.

Acknowledgments

References

1. Mair, W. A. (1969). Reduction of base drag by boat-tailed afterbodies in low speed flow. *Aeronautical Quanterly*, *20*, pp. 307-320.

2. Tanner, M. (1984). Steady base flows, *Progress in Aerospace Sciences*, *21*, 81-157.

3. Mair, W. A. (1978). Drag-Reducing Techniques for Axisymmetric Bluff Bodies. in *Proceedings on the Symposium on Aerodynamic Drag Mechanisms of Bluff Bodies and Road Vehicles*, Edited by Sovran, G., Morel, T., Mason, W.T., General Motors Research Laboratories, Plenum Press, New York.

4. Viswanath, P. R. (1991). Flow management techniques for base and afterbody drag reduction. *Progress in Aerospace Sciences*, *32*, pp. 79-129.

5. Buresti, G., Iungo, G. V., Lombardi, G. (2007). Method for the drag reduction of bluff bodies and their application to heavy road - vehicles, *1st Interim Report Contract between CRF and DIA*, DDIA, 10-2007.

6. Mariotti, A. and Buresti, G. Gaggini, G., Salvetti, M.V. (2017). Separation control and drag reduction for boat-tailed axisymmetric bodies through contoured transverse grooves. *Journal of Fluid Mechanics*, *832*, 514-549.

7. Mariotti, A. (2017). Axisymmetric bodies with fixed and free separation: Base-pressure and near-wake fluctuations. *Journal of Wind Engineering and Industrial Aerodynamics*, *176*, 21-31.

8. Tran, T. H., Ambo, T., Lee, T., Chen, L., Nonomura, T. Asai, K. (2018). Effect of boattail angles on the flow pattern on an axisymmetric afterbody at low speed. *Experimental Thermal and Fluid Science, 99*, 324-335.

9. Tran, T. H., Ambo, T., Lee, T., Ozawa, K., Chen, L., Nonomura, T., Asai, K. (2019). Effect of Reynolds number on flow behavior and pressure drag of axisymmetric conical boattails in low-speed conditions. *Experiments in Fluids*, *60*(3).

10. Tran, T. H., Ambo, T., Chen, L., Nonomura, T. Asai, K. (2019). Flow filed and aerodynamic force analysis of axisymmetric afterbodies under low-speed condition, *Transactions of Japan Society for Aeronautical and Space Sciences*, *62*(4), pp. 219-226.

11. Gentile, V., Schrijer, F. F. J., Oudhcusden, B. W., Scarano, F. (2016). Afterbody effects on axisymmetric base flows. *AIAA Journal*, *6*.

12. Westerweel, J., Geelhoed, P. F., Lindken, R. (2004). Single-Pixel Resolution Ensemble Correlation for Micro-PIV Applications. *Experiments in Fluids, 37*, pp. 375-384.

13. Kahler, C. J., Scholz, U., Ortmanns, J. (2006). Wall-shear-stree and near-wakk turbulence measurements up to single pixel resolution means of long-distance micro-PIV. *Experiments in Fluids*, *41*, pp. 327-341.

14. Lavrukhin, G. N., Popovich, K. F. (2009). *Aero-gazadynamics of jet nozzles - flow around the base* (Vol. 2), TSAGI, Moscow Russia (written in Russian).

15. Mariotti, A. and Buresti, G. (2013). Experimental investigation on the influence of boundary layer thickness on the base pressure and near-wake flow features of an axisymmetric blunt-based body. *Experiments in Fluids, 54*, 1612.

16. Karman, Th. V. (1930). Mechanical Similitude and Turbulence. *NACA Technical Memorandums*, *611*.

ỨNG DỤNG THUẬT TOÁN TƯƠNG QUAN TOÀN PHẦN
CỦA TỪNG PIXEL ẢNH CHO VIỆC ĐO LỚP BIÊN
TRÊN BỀ MẶT ĐUÔI ĐỐI XỨNG

Tóm tắt: *Phương pháp đo vận tốc bằng ảnh hạt (PIV) là một kỹ thuật quan trọng cho phân tích trường vận tốc. Tuy nhiên, với thuật toán tương quan toàn phần truyền thống, độ phân giải của trường vận tốc bị giới hạn và rất khó để đo được lớp biên bề mặt. Trong bài báo này, thuật toán tương quan toàn phần từng pixel ảnh được ứng dụng để phân tích dòng sát bề mặt của mô hình đuôi đối xứng. Các ảnh ban đầu được chụp bằng phương pháp thực nghiệm. Kết quả nghiên cứu chỉ ra rằng phương pháp mới cải thiện đáng kể độ phân giải của dòng chảy sát bề mặt vật và có thể sử dụng để đo lớp biên. Các đặc tính cụ thể của lớp biên đối xứng tại điều kiện dòng chảy khác nhau được thảo luận. Lớp biên tại vùng liên kết đuôi tàu và thân vật không thay đổi nhiều trong điều kiện dòng chảy khác nhau. Tuy nhiên, kích thước của vùng xoáy trên bề mặt giảm đáng kể khi tăng số Reynolds. Kết quả của nghiên cứu này có thể hữu ích cho các nghiên cứu mô phỏng số và thực nghiệm tiếp theo trong việc giảm lực cản của vật đối xứng.*

Từ khoá: *Thuật toán tương quan pixel ảnh; PIV; mô hình đuôi; lớp biên.*

❑